Central Lancashire Online Knowledge (CLoK)

Title	Multiscale micromagnetic / atomistic modeling of heat assisted magnetic recording
Type	Article
URL	https://clok.uclan.ac.uk/id/eprint/54457/
DOI	https://doi.org/10.1109/TMAG.2025.3565885
Date	2025
Citation	Gija, Mohammed, Dobrynin, Alexey, McNeill, Kevin, Gubbins, Mark, Mercer, Tim, Bissell, Philip and Lepadatu, Serban (2025) Multiscale micromagnetic / atomistic modeling of heat assisted magnetic recording. IEEE Transactions on Magnetics, 61 (7). ISSN 0018-9464
Creators	Gija, Mohammed, Dobrynin, Alexey, McNeill, Kevin, Gubbins, Mark, Mercer, Tim, Bissell, Philip and Lepadatu, Serban

Multiscale micromagnetic / atomistic modeling of heat assisted magnetic recording

Mohammed Gija* Alexey Dobrynin†, Kevin McNeill†, Mark Gubbins†, Tim Mercer*, Philip Bissell*, Serban Lepadatu*

* Jeremiah Horrocks Institute, University of Central Lancashire, Preston PR1 2HE, UK

†Seagate Technology, 1 Disc Drive, Derry BT48 0BF, Northern Ireland, UK

Abstract—**Heat-assisted magnetic recording (HAMR) is a recent advancement in magnetic recording, allowing to significantly increase the areal density capability (ADC) of hard disk drives (HDDs) compared to the perpendicular magnetic recording (PMR) technology. This is enabled by high anisotropy FePt media, which needs to be heated through its Curie temperature (T_C) to facilitate magnetization reversal by an electromagnetic write pole. HAMR micromagnetic modeling is therefore challenging, as it needs to be performed in proximity to and above T_C, where a ferromagnet has no spontaneous magnetization. An atomistic model is an optimal solution here, as it doesn't require any parameter renormalization or non-physical assumptions for modeling at any temperature. However, a full track atomistic recording model is extremely computationally expensive. Here we demonstrate a true multiscale HAMR modeling approach, combining atomistic spin dynamics modeling for high temperature regions and micromagnetic modeling for lower temperature regions, in a moving simulation window embedded within a long magnetic track. The advantages of this approach include natural emergence of T_C and anisotropy distributions of FePt grains. Efficient GPU optimization of the code provides very fast running times, with a 60 nm wide track of twenty-five 20 nm - long bits being recorded in several hours on a single GPU. The effects of realistic FePt L_{10} vs simple cubic crystal structure is discussed, with the latter providing further running time gains while keeping the advantages of the multiscale approach.**

Index Terms—**Heat assisted magnetic recording, atomistic spin dynamics, multiscale modeling.**

I. INTRODUCTION

HARD disc drives (HDDs) remain the key data storage technology due to their long-term reliability and low cost per GB. The International Data Corporation Global DataSphere Forecast estimated that by 2028 the worldwide data created, captured and duplicated will increase to 394 ZB [1]. Therefore, an increase in efficiency and areal density capability (ADC) is needed to keep up with this demand. The ADC of HDDs is achieved through increasing the bit and track densities, which requires the media grain size reduction, and increase of magnetocrystalline anisototropy to prevent thermal instabilities due to superparamagnetic effects [2], [3]. The 'magnetic recording trilemma' describes the conflicting requirements for recording density, thermal stability and writeability [4]. The requirement of small grain size necessitates an increase in the grain's magnetocrystalline anisotropy, in turn requiring a stronger magnetic field for the grain's reversal, which exceeds that achievable with integrated electromagnetic perpendicular magnetic recording (PMR)

write heads. One possible solution to this, pioneered by Seagate, is using heat assisted magnetic recording (HAMR) [5]. The magnetic track is heated locally by a laser to a temperature above its Curie temperature T_C, thus temporarily removing anisotropy to facilitate the grains' switching within the heated spot [5]. A common recording material used in HAMR is FePt due to the optimal combination of high anisotropy, reasonably good spontaneous magnetization and low Curie temperature of the order of 700 K [2].

Standard micromagnetic modeling is based on numerical solution of Landau-Lifshitz-Gilbert (LLG) equation in the assumption of constant magnetization (macrospin) of a unit cell used for meshing the ferromagnet [6]. Micromagnetic modeling of HAMR recording processes is significantly more complicated due to the recording happening at around T_C and above, where the assumption of constant spontaneous magnetization M_s is not valid. A number of approaches have been used to address this challenge, including Landau-Lifshitz-Bloch (LLB) equation enabling the temperature dependent magnetization vector length [7]–[10] or LLG with renormalized parameters (magnetization, anisotropy, exchange stiffness, damping) at elevated temperatures [11], [12]. Both these approaches require a number of assumptions for HAMR modeling, most importantly, that of some finite M_s value above T_C, which is not physical.

Another approach to modeling of magnetic materials is atomistic spin dynamics (ASD), which implies localisation of electrons, confining the magnetic moment in the crystal lattice sites [13]. This is a perfectly valid assumption for local ferromagnets, but it was demonstrated that itinerant 3d magnetic materials are also well described by this phenomenology [14]. An atomistic magnetic moment is always constant in ASD, and the materials' temperature dependent parameters, including the ordering temperature T_C, naturally emerge due to accurate inclusion of stochasticity.

An important use of ASD is to understand the effects of finite size on the properties of FePt. In particular, the distribution of T_C has been investigated, and it was found that a rapid decrease in T_C is obtained as the grain size of FePt becomes smaller [15]. ASD modeling has also been used to discover other important factors for HAMR such as the damping mechanism which was found to rapidly increase

as it approaches T_C and is further enhanced by reduction in grain size [16]. This makes using ASD for HAMR modeling even more beneficial, since it allows accurate modeling of thermal gradients and transition jitter effects, which depend on the grains' T_C and anisotropy distribution, and which determine media signal-to-noise ratio, bit error rate (BER), and other important recording parameters [17]–[19]. It should be noted that renormalized magnetic parameters, computed numerically and imported into a micromagnetic model based on the LLG equation [11], also allowed computation of a number of important HAMR performance characteristics, including transition jitter, in quantitative agreement with atomistic approaches. Another important advantage of the atomistic discretization is the more realistic description of the structure and shape of small grains and their boundaries in high ADC media. The biggest disadvantage of atomistic modeling is the required computational power and time, making purely atomistic models not usable for recording real size tracks. Limited multiscale usage of HAMR processes have been previously explored [20], [21], where an atomistic model was used to parameterize a micromagnetic model.

In our work, we propose a true multiscale model, where simultaneous atomistic and micromagnetic modeling regions are used inside a moving simulation window, embedded within a granular magnetic track. This approach excels since the atomistic region is reserved for high temperatures around T_C, whereas the micromagnetic regions with temperature-dependant magnetic parameters are reserved for the lower temperature regions. This multiscale HAMR track writing algorithm is developed to demonstrate the bit writing process required for data storage, implemented in the multiscale micromagnetic/atomistic modeling software BORIS [22] using graphical processing units (GPU). This approach is favourable as it utilises crucial aspects of each modeling type whilst reducing the drawbacks, such as excessive computation time and inaccuracy.

II. HAMR Multiscale Algorithm

HAMR modeling is implemented in the following way – a high temperature spot (either introduced inside the model or imported from an external simulation) overlapping a writer's magnetic field profile is moved along a granular magnetic track of exchange-decoupled FePt grains, obtained by Voronoi construction, with a set velocity, and a bit sequence written by changing the magnetic field polarity. This may be done with a micromagnetic formalism, or using ASD modeling. The problem with either approach is the size of the simulation mesh required for writing long bit sequences, as needed to determine BER [23] for example, which results in unacceptably long simulation times. Moreover, if thermally activated magnetic switching events, and distributions of temperature-dependent magnetic parameters are to be included accurately, particularly as the temperature approaches and exceeds T_C, the ASD formalism is preferable. However, ASD simulations can be over an order of magnitude slower than micromagnetic simulations. Here

we solve both these problems by introducing a multiscale HAMR track writing algorithm, as depicted in Fig. 1.

A simulation window is defined, which is embedded in a long magnetic track. The temperature and external magnetic field profiles are centred in the simulation window, which moves along the track at a set velocity in steps set by the track discretization cellsize. The magnetic track is effectively frozen, thus the computational cost is set by the size of the simulation window alone, and not by the length of track being written. As the simulation window moves, magnetization is transferred from the track to the window at the leading end, and written magnetic information is transferred from the simulation window to the track at the trailing end. Whilst the magnetic track is frozen, the stray field generated by it is fully computed when the simulation window is shifted, and included in the simulation window at each iteration. Moreover, the ends of the simulation window are exchange coupled to the track (further details below). The simulation window can consist of a single computational mesh – either fully micromagnetic or fully atomistic – or multiple meshes. Thus, the simulation window itself can be multiscale, and an effective configuration here consists of a central atomistic mesh which contains the high temperature region, with micromagnetic meshes either side for the lower temperature regions, exchange coupled to the atomistic mesh, and with the stray field between meshes fully computed each iteration. The atomistic mesh can be defined with any crystal structure required, and here we investigate the simple cubic (SC) structure, as well as the realistic L_{10} structure for FePt [24], with unit cell detailed in Appendix A. Inside the atomistic mesh the magnetic spins are evolved using the stochastic LLG (sLLG) equation [25]:

$$\frac{\partial \mathbf{m}}{\partial t} = -\gamma \mathbf{m} \times (\mathbf{H} + \mathbf{H}_{th}) + \lambda \mathbf{m} \times \frac{\partial \mathbf{m}}{\partial t} \quad (1)$$

Here $\mathbf{m}$ is the magnetic spin direction, λ is the damping, and γ is the gyromagnetic ratio. The thermal stochastic field, $\mathbf{H}_{th}$, is generated using a normal distribution with zero mean and standard deviation $\sqrt{2\lambda k_B T/\gamma \mu_0 \mu_S \Delta t}$, where μ_S is the magnetic moment, T is the temperature and Δt is the integration time-step. In the micromagnetic regions either the micromagnetic LLG equation [11] – same form as Equation (1), but without the stochastic field – or the Landau Lifshitz Bloch (LLB) [7] is solved, which additionally contains a longitudinal relaxation term, and here we investigate both. In the micromagnetic regions it is further necessary to impose temperature dependences of magnetic parameters. These are $M_S(T) = M_S^0 m_e(T)$ for the spontaneous magnetization, $A(T) = A_0 m_e^2(T)$ for the exchange stiffness [26], $K(T) = K_0 m_e^3(T)$ for the uniaxial anisotropy constant [27], and $\alpha = \lambda(1 - T/3T_C)$ for the micromagnetic Gilbert damping with $T < T_C$. Note, the micromagnetic damping term coincides with the atomistic damping term at 0 K, with the latter being independent of temperature. Here $m_e(T) = B[m_e 3T_C/T + \mu_S \mu_0 H_{ext}/k_B T]$ is the equilibrium magnetization scaling function, where T_C is the Curie temperature, H_{ext} is the external magnetic field magnitude, and $B(x) = coth(x) - 1/x$ is the Langevin
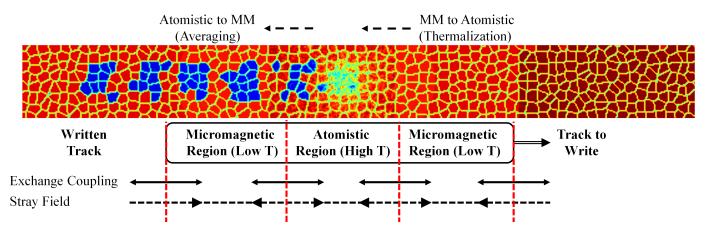
Fig. 1. Diagram of multiscale HAMR modeling track writing algorithm, with a simulation region embedded within a granular magnetic track. The simulation region consists of a central atomistic modeling region for higher temperatures, with left and right micromagnetic modeling regions for lower temperatures, with region boundaries indicated by vertical dashed lines. All regions are exchange-coupled across the boundaries and with stray field contributions fully computed. The simulation region moves along the track at a set velocity, with magnetization from the micromagnetic region transferred to magnetic moments in the atomistic region using a thermalization process, and magnetic moments from the atomistic region transferred to magnetization in the micromagnetic region using averaging.

function. An advantage of ASD modelling is the natural emergence of magnetic parameters temperature dependences, whilst for micromagnetic modelling these must be enforced using approximate relations as given above, and thus use of an atomistic modelling window in the multiscale algorithm leads to more accurate results. Another option for micromagnetic modelling is computation of temperature dependences using atomistic modelling [20], [21], or use of empirical data to introduce temperature dependences.

In the atomistic simulation region the effective field $\mathbf{H}$ in Equation (1) contains a number of contributions, including direct exchange, uniaxial anisotropy, stray field from the track and micromagnetic regions, demagnetizing field (here approximately the same as the field due to dipole-dipole interaction), as well as the external write field. The direct exchange field at a spin i is given in Equation (2), where the sum runs over the neighbours $j \in N$, and $J = J_{ij}$ is the exchange energy. For the SC structure the 6 nearest neighbours are considered. For the L_{10} FePt structure the 4 nearest neighbours, as well as the 6 next nearest neighbours are included.

$$\mathbf{H}_{exch,i} = \frac{1}{\mu_0 \mu_S} \sum_{j \in N} J_{ij} \mathbf{m}_j \qquad (2)$$

The uniaxial anisotropy interaction field is given in Equation (3), where K_1 is the anisotropy energy and $\mathbf{e}_A = \hat{\mathbf{z}}$ is the perpendicular anisotropy axis direction.

$$\mathbf{H}_{an,i} = \frac{2K_1}{\mu_0 \mu_S} (\mathbf{m}_i \cdot \mathbf{e}_A) \mathbf{e}_A \qquad (3)$$

In the micromagnetic region these interactions become the micromagnetic exchange interaction – Equation (4) – and the micromagnetic uniaxial anisotropy interaction – Equation (5).

$$\mathbf{H} = \frac{2A}{\mu_0 M_S} \nabla^2 \mathbf{m} \qquad (4)$$

$$\mathbf{H} = \frac{2K}{\mu_0 M_S} (\mathbf{m} \cdot \mathbf{e}_A) \mathbf{e}_A \qquad (5)$$

For exchange coupling the atomistic and micromagnetic regions Equations (2) and (4) are used, respectively. Equation (4) is evaluated in a finite-difference implementation with a 6-neighbor stencil for the Laplacian operator. For the contribution from the atomistic region the average atomistic spin direction is obtained in the respective stencil cell. For the contribution from the micromagnetic region the respective magnetization direction is used directly since the atomistic lattice constant is smaller than the micromagnetic cellsize.

When transferring from an atomistic to a micromagnetic region the micromagnetic magnetization vector $\mathbf{M}$ is obtained as the sum of atomistic magnetic moments divided by the micromagnetic cellsize volume V, as shown in Equation (6).

$$\mathbf{M} = \frac{\mu_S}{V} \sum_{j \in V} \mathbf{m}_j \qquad (6)$$

When transferring from a micromagnetic to an atomistic region, the same Equation (6) is used, but now as an inverse problem. The atomistic spins are generated using a uniform distribution of the polar angle from the magnetization vector direction, inside a cone with a set maximum angle. The maximum angle required to reproduce the correct micromagnetic magnetization magnitude M is obtained as $\theta_{max} = (5\pi/9)\sqrt{1 - \sqrt{1 + 6(M/M_S^0 - 1)/5}}$, where M_S^0 is the magnetization at zero temperature, obtained in the ground state when all the atomistic spins are aligned. It is known that the normalized magnetization length decreases with temperature, as shown by the Monte Carlo simulation in Appendix B, Fig. 8. Thus, the choice of this cone angle is set so the correct magnetization length is obtained by averaging the uniformly distributed atomistic spins. In reality, the atomistic spins do not have a uniform distribution - see e.g. Ref. [28] - however, the correct distribution is obtained

by iterating the sLLG equation, and the uniform distribution serves as a starting point for this thermalization process. We have tested methods where the thermalization is completed using the sLLG equation as part of the main simulation, but also separately, and with the simulation back-tracked so it proceeds with an accurately thermalized spin distribution. We have found no differences between the two methods thus, the former, more computationally efficient method, is used here.

For micromagnetic regions the demagnetizing field is computed using Equation (7), using the standard approach of a convolution sum with the demagnetizing tensor $\mathbf{N}$ [29].

$$\mathbf{H}_{d,i} = -\sum_j \mathbf{N}(\mathbf{r}_j - \mathbf{r}_i)\mathbf{M}_j \qquad (7)$$

For atomistic regions, rather than using the dipole-dipole interaction, the same Equation (7) is used, where the atomistic magnetic moments are first transferred to the coarser micromagnetic discretisation using Equation (6). As we have verified the demagnetizing field obtained using Equation (7) is approximately the same as that obtained using the more expensive dipole-dipole interaction. This approach also allows computation of the stray field between multiple micromagnetic and atomistic meshes, which is done using the multilayered convolution algorithm previously introduced [30], [31]. Thus, within the simulation region the demagnetizing and stray fields are re-computed at every iteration, whilst the stray field contribution from the track is updated only when the simulation region moves. The algorithm has been implemented for central processing units, single GPUs, as well as multiple GPUs [31].

III. HAMR SIMULATIONS

Employing atomistic modeling in HAMR simulations could reveal previously hidden interactions between the heating of the medium and magnetization reversal. Therefore, multiscale modeling is a favourable approach since the temperatures will be extreme at the centre of the laser spot, whereas the outer areas will have a lower temperature which is adequately described by micromagnetic modeling. This section outlines the results obtained from these various types of modeling.

The HAMR simulations for this paper were performed using idealized temperature and field profiles, plotted in Fig. 2. This figure shows the Gaussian temperature profile due to a laser spot, used to heat the magnetic track above T_C. Fig. 2 has a horizontal marker (dotted red line) to indicate T_C at 710K, and the laser spot diameter above T_C was 25 nm, which largely determined the width of written bits. The magnetic field from the write pole was simulated as $tanh$ profiles along the track, both for the out-of-plane and in-plane field components shown in Fig. 2. As the shape and positioning suggest, the field is used to reverse the grains which have been heated. The field strength is not required to be large due to the decrease in coercivity from heating, so unheated grains are not reversed, with spatial resolution provided by the temperature spot.
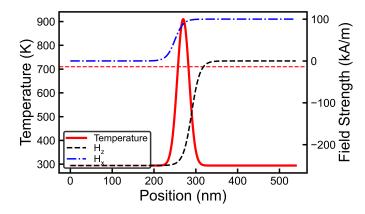

Fig. 2. Plot of the Gaussian temperature profile due to the laser spot (solid red line), shown along the track, with a horizontal dashed red line to indicate the Curie temperature at 710 K. The black dashed line shows the out-of-plane component (H_z) of the field profile along the track, whilst the dash-dot blue line shows the in-plane component (H_x).

The magnetic tracks used throughout the simulations had dimensions of 540 nm $\times$ 60 nm $\times$ 16 nm with cell sizes of 1 nm $\times$ 1 nm $\times$ 2 nm, and a grain size of 8 nm, with a simulation window length of 300 nm. Arbitrarily long tracks may be set, without increasing the time per iteration. However, this track length was sufficient to accommodate a varied bit pattern. Atomistic simulations had a SC structure with lattice constant a = 0.5 nm. Other grain sizes of 7 nm and 9 nm were also simulated. The laser spot moved along the track at a velocity of 20 m/s, comparable to the linear velocity in a physical HDD.

For the atomistic models, the exchange energy for the spin moments was obtained by using the desired T_C of 710 K in conjunction with Equation (8). However, the mean-field correction factor (ϵ) is unknown, so to obtain a value for this and thus the exchange energy, Monte Carlo modeling was used [32]. The mean-field correction factor is dependent on the crystal structure. The resulting mean-field correction factors were determined to be ϵ_{SC} = 0.72 and ϵ_{L10} = 0.78 for SC and L_{10} respectively, obtaining exchange energies $J_{SC} = 6.8 \times 10^{-21}J$ and $J_{L10} = 3.77 \times 10^{-21}J$. The co-ordination number (z) for SC is 6 and 10 for L_{10}. In this work, the exchange energy was set to be identical for all included neighbors. However, further work could use a more advanced model to take into account the varying J values of the nearest and further distant neighbors. [33]

$$J = \frac{3k_B T_C}{\epsilon z} \qquad (8)$$

For micromagnetic simulations, the exchange energy is related to exchange stiffness A, as shown in Equations (9) and (10) for SC and L_{10} respectively. As shown in Appendix A, we have verified using spin-wave dispersion simulations that the implemented exchange interactions for SC and L_{10} crystal structures are correct.

$$A_{SC} = \frac{J}{2a} \qquad (9)$$

$$A_{L10} = \frac{3J}{2a} \tag{10}$$

The M_S and K micromagnetic parameters were used as $5.2 \times 10^5 A/m$ and $2.2 \times 10^6 J/m^3$ respectively. These micromagnetic parameters also have a temperature dependence as given in the previous section. A damping value of 0.1 (at 0 K) was used for both atomistic and micromagnetic regions, with the latter also having a temperature dependence as described above.

Fig. 3 shows the results of the multiscale algorithm described in Fig. 1. The atomistic central window used a SC crystal structure while the windows on either side were micromagnetic LLG. The grain sizes were not uniform along the track, with many being larger or smaller than the nominal value of 8 nm. This causes a distribution in temperature dependence along the track which means that there is a distribution in T_C. The micromagnetic track in Fig. 3 has been simulated with a T_C distribution, in particular a normal distribution with standard deviation about T_C = 710 K of $0.05 \times T_C$. For comparison purposes the bit pattern to be written was kept consistent throughout all simulations. The bit pattern used was 001011110010110110100001 and the bit length was 20 nm. The red grains represent the out-of-plane direction, the blue grains represent the reversed into-the-plane direction, and the green areas represent empty space. The modeled region was 60 nm (cross-track) by 540 nm (down-track), and the obtained track width in both cases was about 25 nm, as defined by the temperature profile. Here, the atomistic and the two micromagnetic window lengths were all 100 nm. In terms of accuracy, by comparing the TMR read-head patterns, it was found the atomistic window should cover a region with a minimum temperature T_C - 100 K or smaller, while the micromagnetic regions should extend to a minimum temperature of 100 K above room temperature, or smaller.

A simulated TMR read-head was used to read the information stored on the track. This read-head traversed the tracks along its length and converted the stray field due to the out-of-plane magnetization to a resistance value. The TMR read-head consists of a magnetic tunnel junction sensor on top of a synthetic antiferromagnetic (SAF) stack and with magnetic shields, as described in Ref. [34]. These data sets are plotted in Fig. 3(b). This plot shows that the overall pattern is in line with the expected bit pattern and is similar to the micromagnetic result. The conventional way to assess recording quality is to perform analysis on multiple waveforms, obtained from many pseudo-random bit sequence (PRBS) tracks [35]. This allows to capture key parameters, characterizing the recorded bit quality and the bit transition region, including remanent and transition SNR, bit error rate, etc. The multiscale method excels in these circumstances, as at high temperatures atomistic modeling is the only proper way to take stochasticity into account. The purpose of this manuscript is to present the modeling technique by using artificial field and temperature profiles, rather then providing real HAMR quantitative track analysis. Therefore, quantitative recording subsystem analysis including real magnetic writer

field and near field transducer's heat profiles, is not included here, as it would be subject of a separate work. However, from the visual comparison of multiscale and micromagnetic tracks shown in Fig. 3, both simulations resulted in tracks with very similar recordings. The pre-defined bit pattern is consistent through both images and follows the expected sequence. However, there are two consistent differences. One, as observed in Fig. 3(b), the reader pattern obtained from the micromagnetic HAMR track consistently lags behind that obtained from the multiscale track. This is due to different threshold temperatures required to obtain grain switching in atomistic modelling, compared to the less accurate micromagnetic model with enforced magnetic parameter temperature dependences. In particular, with ASD grain switching is obtained at lower temperatures compared to the micromagnetic model, resulting in approximately 1 grain shift to the left. Another difference is apparently slightly worse quality of both bits and transitions in the multiscale case. This is not unexpected, as the atomistic / multiscale approach allows to accurately take into account stochastic effects at hight temperatures, as discussed above. This is further evidenced by simulations with 7 nm and 9 nm grain sizes. These results show that the larger the grain size, the fewer thermally activated switched grains are present. Such thermally activated switching occurs only in the vicinity of T_C for ASD / multiscale modeling owing to stochasticity introduced in the LLG equation. For comparison purposes, micromagnetic simulations were run using LLG and LLB equations. Stochastic micromagnetic modeling is also possible. However, this is beyond the scope of the current work. Both equations induce switching using the transverse damping term but the main difference in these approaches is the existence of a longitudinal relaxation term in LLB, which is particularly important in the ultrafast time regime. In the simulations, the parameters changed between methods was the time-step used to solve the equations using the RK4 method. LLB required a significantly smaller timestep of 2.5 fs whereas LLG needed a 20 fs timestep. This is reflected in the time taken for simulations to complete, which were run on a single A5000 GPU. LLG, with the larger time-step, completed the simulation in approximately 40 minutes whereas LLB took 440 minutes. Detailed benchmarking results for the different models are shown and discussed in Appendix B. The resulting simulations showed that the different equations do not differ significantly in clarity of writing bits. Considering the significant additional time taken for LLB simulations and the dominant precessional switching at this timescale, we proceeded to use LLG for the micromagnetic regions in the multiscale algorithm.

In the same manner, atomistic crystal structures of SC and L_{10} were compared to investigate the advantages and disadvantages of using realistic FePt L_{10}. L_{10} required a smaller time-step of 5 fs as the solution diverged when using the same time-step of SC at 10 fs. The time taken for completion of SC simulation was approximately 295 minutes and 1686 minutes for L_{10}. The simulations resulted in similar tracks with minor differences which can be accounted for by
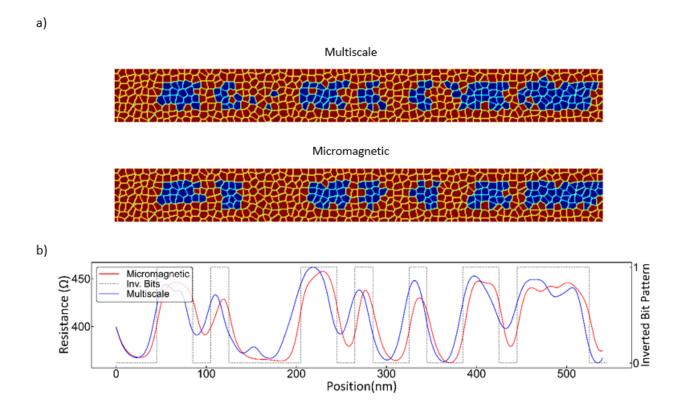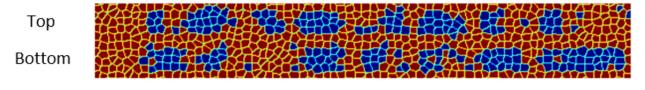
a)

Fig. 3. a) Written bit patterns on a granular track with 8 nm grain size, for a uniform out-of-plane magnetized initial state (red), shown for multiscale and micromagnetic LLG simulations. The into-the-plane grains (blue) represent reversed grains. b) Plots of a TMR read-head scan obtained for the respective bit patterns shown in a), with the inverted bit pattern also plotted.

thermally activated switching. In terms of efficiency, SC is the reasonable crystal structure to use for multiscale simulations. However, further work is needed to investigate the effect of crystal structure and exchange constants parameterization in Equation (2). An important difference between SC and L_{10} is the longitudinal magnetic susceptibility, which, as shown in Appendix A, is around one order of magnitude smaller for L_{10}. This may be important if ultrafast processes are considered, however in the present case where precessional switching dominates, the results obtained show the SC structure is sufficient. For the multiscale modeling algorithm, the 300 nm long simulation window is split between a 100 nm long atomistic simulation region and two 100 nm long micromagnetic simulation regions. With an SC structure, the simulation time was 228 minutes, which is a modest decrease compared to a fully SC atomistic window. However, the performance is strongly dependent on the size and complexity of the problem. For example, with the more complex L_{10} atomistic region, the multiscale algorithm completed in 459 minutes, which is between three to four times faster compared to a fully L_{10} atomistic window. The algorithm can be further sped up using multiple GPUs, which is particularly beneficial for large simulation windows [31]. Even for the current relatively small simulation windows, a further speedup factor up to 40% is achieved with $2 \times$ A5000 GPUs.

Finally, the multiscale track shifting algorithm is applied for writing parallel tracks, with results shown in Fig. 4 for two parallel tracks. Here, the bits are approximately 25 nm wide as before, with the separation between tracks being 15 nm, for a total simulation window with 80 nm width. The two tracks were written sequentially. Starting from the uniform magnetization state, the bottom track was written first as before, achieved by positioning the laser spot in the centre of the bottom track. The written bit pattern was then used as the starting state for a second pass through the track shifting algorithm, this time writing a different bit pattern in the top track. The respective bit patterns are shown in Fig. 4(b) and Fig. 4(c) for the top and bottom tracks respectively. The TMR read-head scans show that the written bit patterns were reproduced, with transitions between bits clearly identified. Thus, the multiscale track shifting algorithm developed here can also be used to study the effect of writing multiple parallel tracks. Whilst the 15 nm separation between tracks does not affect previously written bit patterns, with the read-head scan resolution also preserved, further studies can be conducted to investigate the effect of reducing track-track separation, or even shingled magnetic recording, in order to identify acceptable operating parameters as the areal density is increased. While in the current work the grains are exchange decoupled, future work can include recording media with weakly exchange-coupled grains. The multiscale algorithm
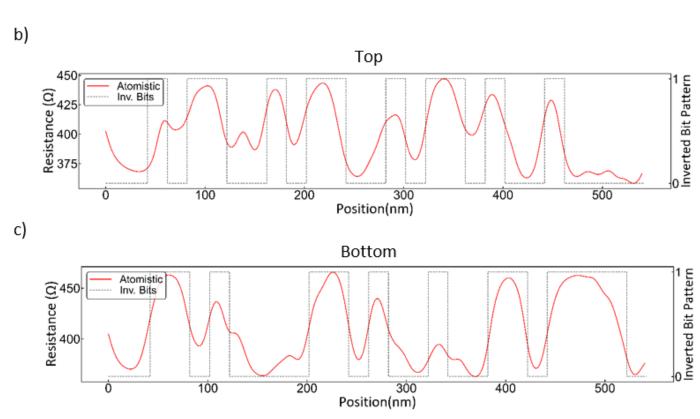
a)

b)

c)

Fig. 4.   a) Written bit patterns with two tracks. The into-the-plane grains (blue) represent reversed grains. Plots of a TMR read-head scan obtained for the respective bit patterns shown in a), with the inverted bit pattern also plotted for b) top track, and c) bottom track.

discussed here is also applicable to this case, particularly as exchange coupling between grains may be accurately introduced in the atomistic region through magnetic spins which bridge neighboring grains. Further, this multiscale method may be used to compute important HAMR performance characteristics, including transition jitter, which has been shown to result both from stochasticity and grain irregularity [11].

IV. CONCLUSION

In summary, through this work, the concept of using a multiscale algorithm combining atomistic and micromagnetic modeling has been demonstrated by simulating the bit writing process in HAMR on a simulated FePt track, both on single tracks as well as parallel tracks. The simulations were quantitatively analysed through a simulated TMR read-head. An atomistic modeling region was used for higher temperatures around the laser spot, whilst micromagnetic regions were used for lower temperatures either side of the atomistic region. This multiscale approach is favourable due to the additional

accuracy compared to purely micromagnetic simulations, as atomistic modeling at higher temperatures naturally includes the effects of stochasticity, suitable both for the ferromagnetic and paramagnetic phases below and above the Curie temperature respectively. Atomistic modeling at higher temperatures accurately includes the effect of thermally activated grain switching during the HAMR bit writing process, which was found to be dependent on the grain size. Moreover, the general purpose multiscale HAMR track writing algorithm developed here, and implemented in the micromagnetic/atomistic multiscale software BORIS, allows the atomistic modeling region to be configured with a realistic crystal structure, depending on the material investigated, as well as any configuration of exchange interactions between neighbors. Here, we have investigated the L_{10} FePt crystal structure, and compared it to the simpler SC structure, and whilst the written bit patterns did not differ between the two approaches, further studies using the multiscale algorithm developed here could benefit from inclusion of advanced atomistic modeling regions. On

This article has been accepted for publication in IEEE Transactions on Magnetics. This is the author's version which has not been fully edited and content may change prior to final publication. Citation information: DOI 10.1109/TMAG.2025.3565885

8

the other hand, inclusion of micromagnetic modeling regions allows a larger simulation window to be defined, with reduced computation time compared to a purely atomistic modeling approach.

V. APPENDIX A

For atomistic modeling two crystal structures were considered: simple cubic (SC) and L_{10}-ordered FePt – the latter is shown in Fig. 5. Here we only model the Fe atomic sites, with their magnetic moments set such that $M_S = 520 \times 10^5 A/m$ is obtained. For SC this means $\mu_S = M_S a^3$, whereas for FePt L_{10} we have $\mu_S = M_S a^3/2$, since each unit cell contains 2 Fe atoms. Similarly, for the micromagnetic uniaxial anisotropy energy density $K = 2.2 \times 10^6 J/m^3$, we have $K_1 = Ka^3$ for the SC anisotropy energy, and $K_1 = Ka^3/2$ for FePt L_{10}.
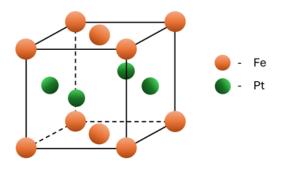

Fig. 5.   Schematic diagram of a L_{10}-ordered FePt crystal lattice.

To ensure the exchange coupling and exchange stiffness values used are correct, we simulated spin-wave dispersions to corroborate simulation results to theoretical expectations. The methodology used is outlined in [36]. This was done in BORIS by using a thin magnetic material with dimensions of 1000 nm x 50 nm x 1 nm, on which a $sinc$ pulse was used to excite spin-waves in the frequency domain in the forward volume (FV) geometry. The FV geometry describes the wavevector along the longitudinal direction and the bias field in the out-of-plane direction, perpendicular to the wavevector. The spin-wave dispersions are parabolic in the frequency–wavevector ($f - k$) space as described by Equation (11). These equations are important as they outline the relationship needed to verify the exchange values used. The exchange factor, λ_{ex}, depends on the exchange stiffness, A, which is directly proportional to the exchange coupling. A further consequence is the dependance on crystal structure due to varying lattice geometry shown in Equations (9) and (10) for SC and L_{10} respectively. Fig. 6 displays the obtained heat map for the dispersion curves of the two crystal structures with the theoretical curves superimposed as red dots. The results show that theoretical and simulated curves align well, verifying the implemented exchange interaction.
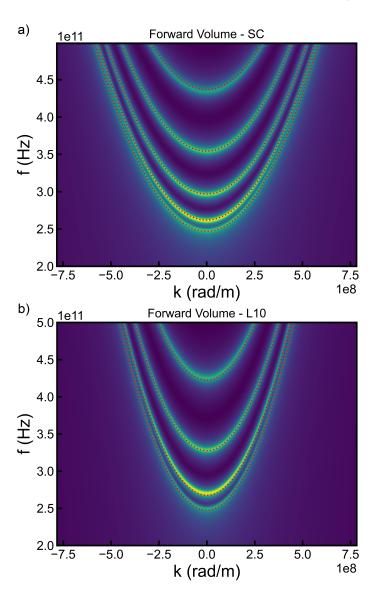

Fig. 6.   Heat map displaying the obtained dispersion curves from spin-wave excitations in the forward volume for SC and L_{10} crystal structures.

$$\omega_{ex} = \omega_0 + \lambda_{ex}\gamma M_S k^2,$$
$$\lambda_{ex} = 2A/\mu_0 M_s^2 \tag{11}$$

The longitudinal magnetic susceptibility is an important property to investigate when looking at a magnetic material. This property determines how sensitive the magnetization length is to external applied fields such as the one used in HAMR, therefore, in this work we modelled the longitudinal magnetic susceptibility of L_{10} and SC crystal structures. This was done using a Monte Carlo algorithm implemented in BORIS, as described previously [32], with results shown in Fig. 7. It was found that there is an order of magnitude difference between the susceptibilities of L_{10} and SC, which is particularly important in the ultrafast regime where longitudinal magnetization switching processes are important. However, for HAMR modeling where precessional switching dominates, it was determined that the use of realistic crystal structure has a negligible effect on the outcome of the written bit pattern.

This article has been accepted for publication in IEEE Transactions on Magnetics. This is the author's version which has not been fully edited and content may change prior to final publication. Citation information: DOI 10.1109/TMAG.2025.3565885

9

For this reason the SC crystal structure is preferable for HAMR modeling due to significantly decreased computation time. A corresponding normalized magnetization temperature dependence, computed using the Monte Carlo algorithm, with the fitted T_C value, is shown in Fig. 8.
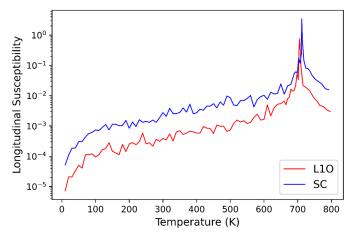

Fig. 7. Longitudinal magnetic susceptibility of SC and L_{10} ordered crystal structures, plotted on a logarithmic scale.
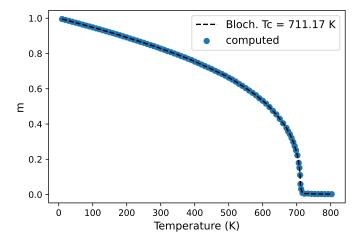

Fig. 8. Normalized magnetization temperature dependence with fitted T_C value.

VI. APPENDIX B

Computational benchmarking results are shown in Fig. 9, comparing micromagnetic, multiscale, and atomistic models. The computations were run using A5000 GPUs, for both 1 and 2 GPUs in parallel. As expected, the micromagnetic model is significantly faster. On the other hand, the multiscale model is up to 2.5 times faster compared to the atomistic model, whilst still maintaining the benefits of atomistic modeling discussed above. The atomistic and multiscale models are efficiently sped up using 2 GPUs for larger problem sizes, where GPU latencies are relatively negligible. Here, for the multiscale model benchmarking, the simulated volume is divided into three regions of equal volume: a central atomistic region, and two micromagnetic regions either side.
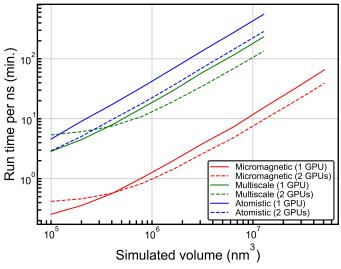

Fig. 9. Benchmarking of different HAMR models, showing run time in minutes per simulated nanosecond, using 1 or 2 GPUs, as a function of simulated volume size.

REFERENCES

[1] IDC, "IDC Market Forecast: Worldwide Digital Commerce Applications Forecast, 2024-2028," International Data Corporation," Market Forecast, 2024. [Online]. Available: https://www.idc.com/getdoc.jsp?containerId=US52076424

[2] C. Jongjaihan and A. Kaewrawang, "Micromagnetic simulation of l10-fept-based transition jitter of heat-assisted magnetic recording at ultrahigh areal density," *Micromachines*, vol. 13, no. 10, pp. 1–28, 2022.

[3] V. Marghussian, "4 - magnetic properties of nano-glass ceramics," *William Andrew Publishing*, p. 181–223, 2015.

[4] Y. Chen and R. H. Victora, "Effectiveness of a pulsed laser in heat-assisted magnetic recording,," *Scientific Reports*, vol. 13, no. 1, 2023.

[5] M. H. Kryder, E. C. Gage, T. W. McDaniel, W. A. Challener, R. E. Rottmayer, G. Ju, Y.-T. Hsia, and M. F. Erden, "Heat assisted magnetic recording," *Proceedings of the IEEE*, vol. 96, no. 11, pp. 1810–1835, 2008.

[6] J. Fidler and T. Schrefl, "Micromagnetic modelling - the current state of the art," *Journal of Physics D: Applied Physics*, vol. 33, no. 15, p. R135, aug 2000. [Online]. Available: https://dx.doi.org/10.1088/0022-3727/33/15/201

[7] D. A. Garanin, "Fokker-planck and landau-lifshitz-bloch equations for classical ferromagnets," *Phys. Rev. B*, vol. 55, pp. 3050–3057, Feb 1997. [Online]. Available: https://link.aps.org/doi/10.1103/PhysRevB.55.3050

[8] D. A. Garanin and O. Chubykalo-Fesenko, "Thermal fluctuations and longitudinal relaxation of single-domain magnetic particles at elevated temperatures," *Phys. Rev. B*, vol. 70, p. 212409, Dec 2004. [Online]. Available: https://link.aps.org/doi/10.1103/PhysRevB.70.212409

[9] T. W. McDaniel, "Application of Landau-Lifshitz-Bloch dynamics to grain switching in heat-assisted magnetic recording," *Journal of Applied Physics*, vol. 112, no. 1, p. 013914, 07 2012. [Online]. Available: https://doi.org/10.1063/1.4733311

[10] S. Greaves, H. Muraoka, and Y. Kanai, "Modelling of heat assisted magnetic recording with the landau-lifshitz-bloch equation and brillouin functions," *J Appl Phys*, vol. 117, no. 17, p. 17C505, 2015.

[11] R. H. Victora and P.-W. Huang, "Simulation of heat-assisted magnetic recording using renormalized media cells," *IEEE Transactions on Magnetics*, vol. 49, no. 2, pp. 751–757, 2013.

[12] W.-H. Hsu and R. H. Victora, "Heat-assisted magnetic recording — micromagnetic modeling of recording media and areal density: A review," *J Magn Magn Mater*, vol. 563, p. 169973, 2022.

[13] M. O. A. Ellis, R. F. L. Evans, T. A. Ostler, J. Barker, U. Atxitia, O. Chubykalo-Fesenko, and R. W. Chantrell, "The Landau–Lifshitz equation in atomistic models," *Low Temperature Physics*, vol. 41, no. 9, pp. 705–712, 09 2015. [Online]. Available: https://doi.org/10.1063/1.4930971

[14] R. F. L. Evans, W. J. Fan, P. Chureemart, T. A. Ostler, M. O. A. Ellis, and R. W. Chantrell, "Atomistic spin model

This article has been accepted for publication in IEEE Transactions on Magnetics. This is the author's version which has not been fully edited and content may change prior to final publication. Citation information: DOI 10.1109/TMAG.2025.3565885

10

simulations of magnetic nanomaterials," *Journal of Physics: Condensed Matter*, vol. 26, no. 10, p. 103202, feb 2014. [Online]. Available: https://dx.doi.org/10.1088/0953-8984/26/10/103202

[15] O. Hovorka, S. Devos, Q. Coopman, W. J. Fan, C. J. Aas, R. F. L. Evans, X. Chen, G. Ju, and R. W. Chantrell, "The Curie temperature distribution of FePt granular magnetic recording media," *Applied Physics Letters*, vol. 101, no. 5, p. 052406, 08 2012. [Online]. Available: https://doi.org/10.1063/1.4740075

[16] M. Strungaru, S. Ruta, R. F. Evans, and R. W. Chantrell, "Model of magnetic damping and anisotropy at elevated temperatures: Application to granular fept films," *Phys. Rev. Appl.*, vol. 14, p. 014077, Jul 2020. [Online]. Available: https://link.aps.org/doi/10.1103/PhysRevApplied.14.014077

[17] A. F. Torabi, J. V. Ek, E. Champion, and J. Wang, "Micromagnetic modeling study of thermal gradient effect in heat-assisted magnetic recording (hamr)," *IEEE Transactions on Magnetics*, vol. 45, no. 10, pp. 3848–3850, 2009.

[18] K. Xue and R. H. Victora, "Dependence of hamr transition curvature on bit length," *IEEE Trans Magn*, vol. 58, no. 2, pp. 1–5, 2022.

[19] H. Li and J.-G. Zhu, "The role of media property distribution in hamr snr," *IEEE Trans Magn*, vol. 49, no. 7, p. 3568–3571, 2013.

[20] N. Kazantseva, D. Hinzke, U. Nowak, R. W. Chantrell, U. Atxitia, and O. Chubykalo-Fesenko, "Towards multiscale modeling of magnetic materials: Simulations of fept," *Phys. Rev. B*, vol. 77, p. 184428, May 2008. [Online]. Available: https://link.aps.org/doi/10.1103/PhysRevB.77.184428

[21] A. Meo, W. Pantasri, W. Daeng-am, S. E. Rannala, S. I. Ruta, R. W. Chantrell, P. Chureemart, and J. Chureemart, "Magnetization dynamics of granular heat-assisted magnetic recording media by means of a multiscale model," *Phys. Rev. B*, vol. 102, p. 174419, Nov 2020. [Online]. Available: https://link.aps.org/doi/10.1103/PhysRevB.102.174419

[22] S. Lepadatu, "Boris computational spintronics - high performance multi-mesh magnetic and spin transport modeling software," *J Appl Phys*, vol. 128, p. 243902, 2020.

[23] Y. Jiao, Y. Wang, and R. H. Victora, "A study of snr and ber in heat-assisted magnetic recording," *IEEE Transactions on Magnetics*, vol. 51, no. 11, pp. 1–4, 2015.

[24] J. Park, Y.-K. Hong, S.-G. Kim, L. Gao, and J.-U. Thiele, "Magnetic properties of Fe-Mn-Pt for heat assisted magnetic recording applications," *Journal of Applied Physics*, vol. 117, no. 5, p. 053911, 02 2015. [Online]. Available: https://doi.org/10.1063/1.4907570

[25] J. L. García-Palacios and F. J. Lázaro, "Langevin-dynamics study of the dynamical properties of small magnetic particles," *Phys Rev B*, vol. 58, no. 22, p. 14937–14958, 1998.

[26] U. Atxitia, D. Hinzke, O. Chubykalo-Fesenko, U. Nowak, H. Kachkachi, O. N. Mryasov, R. F. Evans, and R. W. Chantrell, "Multiscale modeling of magnetic materials: Temperature dependence of the exchange stiffness," *Phys. Rev. B*, vol. 82, p. 134440, Oct 2010. [Online]. Available: https://link.aps.org/doi/10.1103/PhysRevB.82.134440

[27] H. B. Callen and E. Callen, "The present status of the temperature dependence of magnetocrystalline anisotropy, and the l(l+1)2 power law," *Journal of Physics and Chemistry of Solids*, vol. 27, no. 8, p. 1271–1285, 1966.

[28] S. Lepadatu, "Micromagnetic monte carlo method with variable magnetization length based on the landau–lifshitz–bloch equation for computation of large-scale thermodynamic equilibrium states," *Journal of Applied Physics*, vol. 130, no. 16, p. 163902, 10 2021. [Online]. Available: https://doi.org/10.1063/5.0059745

[29] A. J. Newell, W. Williams, and D. J. Dunlop, "A generalization of the demagnetizing tensor for nonuniform magnetization," *Journal of Geophysical Research: Solid Earth*, vol. 98, no. B6, pp. 9551–9555, 1993. [Online]. Available: https://agupubs.onlinelibrary.wiley.com/doi/abs/10.1029/93JB00694

[30] S. Lepadatu, "Efficient computation of demagnetizing fields for magnetic multilayers using multilayered convolution," *J Appl Phys*, vol. 126, no. 10, p. 103903, 2019.

[31] ——, "Accelerating micromagnetic and atomistic simulations using multiple gpus," *Journal of Applied Physics*, vol. 134, no. 16, p. 163903, 10 2023. [Online]. Available: https://doi.org/10.1063/5.0172657

[32] S. Lepadatu, G. Mckenzie, T. Mercer, C. R. MacKinnon, and P. R. Bissell, "Computation of magnetization, exchange stiffness, anisotropy, and susceptibilities in large-scale systems using gpu-accelerated atomistic parallel monte carlo algorithms," *Journal of Magnetism and Magnetic Materials*, vol. 540, p. 168460, 2021. [Online]. Available: https://www.sciencedirect.com/science/article/pii/S0304885321007290

[33] R. F. L. Evans, "Atomistic modelling of nanogranular magnetic materials," *PhD Thesis, The University of York*, 2008.

[34] S. Lepadatu and A. Dobrynin, "Self-consistent computation of spin torques and magneto-resistance in tunnel junctions and magnetic read-heads with metallic pinhole defects," *Journal of Physics: Condensed Matter*, vol. 35, no. 11, p. 115801, 2023.

[35] S. Hernández, P.-L. Lu, S. Granz, P. Krivosik, P.-W. Huang, W. Eppler, T. Rausch, and E. Gage, "Using ensemble waveform analysis to compare heat assisted magnetic recording characteristics of modeled and measured signals," *IEEE Transactions on Magnetics*, vol. 53, no. 2, pp. 1–6, 2017.

[36] G. Venkat, D. Kumar, M. Franchin, O. Dmytriiev, M. Mruczkiewicz, H. Fangohr, A. Barman, M. Krawczyk, and A. Prabhakar, "Proposal for a standard micromagnetic problem: Spin wave dispersion in a magnonic waveguide," *IEEE Transactions on Magnetics*, vol. 49, no. 1, pp. 524–529, 2013.